Hindawi
Wireless Communications and Mobile Computing
Volume 2018, Article ID 6916954, 11 pages
https://doi.org/10.1155/2018/6916954

Research Article

Wideband Channel Modeling for mm-Wave inside Trains for 5G-Related Applications

Juan Moreno García-Loygorri,[1] **César Briso-Rodríguez**,[1] **Israel Arnedo**,[2] **César Calvo**,[1] **Miguel A. G. Laso**,[2] **Danping He**,[3] **Florentino Jiménez**,[1] **and Vicente González Posadas**[1]

[1] *TSC Department, ETSIST, Universidad Politécnica de Madrid, Madrid, Spain*
[2] *Universidad Pública de Navarra, Pamplona, Spain*
[3] *Beijing Jiaotong University, Beijing, China*

Correspondence should be addressed to Juan Moreno García-Loygorri; juanmorenogl@diac.upm.es

Received 2 November 2017; Accepted 14 February 2018; Published 15 April 2018

Academic Editor: Dajana Cassioli

Passenger trains and especially metro trains have been identified as one of the key scenarios for 5G deployments. The wireless channel inside a train car is reported in the frequency range between 26.5 GHz and 40 GHz. These bands have received a lot of interest for high-density scenarios with a high-traffic demand, two of the most relevant aspects of a 5G network. In this paper we provide a full description of the wideband channel estimating Power-Delay Profiles (PDP), Saleh-Valenzuela model parameters, time-of-arrival (TOA) ranging, and path-loss results. Moreover, the performance of an automatic clustering algorithm is evaluated. The results show a remarkable degree of coherence and general conclusions are obtained.

1. Introduction

Metro lines are one of the most acknowledged high-density scenarios, as well as stadiums and other large venues. These places are a clear target for 5G mobile [1] deployments, which is intended to provide very large throughputs and ultra-low latencies in dense environments and sustain a high number of simultaneous connections, among others. It is noteworthy that it is possible to have more than 1200 people inside a 120-meter long train, which means around 5 persons/m^2. There are many railway-related applications like Train-to-Ground, Train-to-Train, Train-to-Car, Train-to-Satellite, intratrain communications, and so on, which are usually grouped under the T2X notation, or perhaps in the more generic V2X notation, where "V" stands for vehicular. In this paper we focus on the intratrain channel, which has an enormous importance to provide connectivity to passengers. Also, this wireless channel could be used for the internal communications of the train, which is one of the objectives of the EU-H2020 Roll2Rail Project [2].

There is still some vagueness in the frequency bands to be assigned, but some things are clear: there will be 5G deployments both above and below 6 GHz [3]. This fact has attracted much attention on millimeter waves (mm-wave) in order to have larger bandwidths than in lower frequencies, where the entire spectrum has been allocated. For example, in USA both the 28 GHz (27.5–28.35 GHz) and the 37 GHz band (37–40 GHz) have been licensed for mobile applications; in both China and the European Union, the 26 GHz band (24.25–27.5 GHz) is the chosen one. On the other side, there is no clear direction on which bands will be allocated for unlicensed use, but the 37 GHz band (37–37.6 GHz) is perhaps the most promising one. All these spectrum policies lead to the need of a proper channel model for 5G-related scenarios in the aforementioned bands.

There are many papers related to channel measurements and modeling in railway scenarios but, as far as we know, only very few of them are focused on mm-wave for intratrain environments (i.e., the work carried out by ETRI in Korea [4]). Regarding the Train-to-Ground link for high-speed

(a) (b)

Figure 1: Rolling stock used in the measurements campaign. (a) The train interior and (b) the exterior are shown.

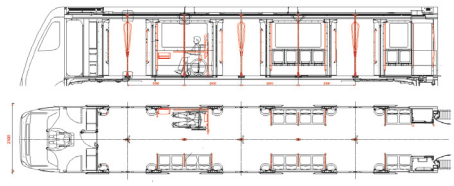

Figure 2: Top and lateral view of one car of the s3000 rolling stock.

trains, a very complete reference is [5] but it is focused on frequencies below 6 GHz; for tunnels which are a very common scenario in railways, there are many papers, like [6, 7]; inside metro stations there are many research papers like [8]; and for mm-wave research in railways there are some ray-tracing simulations in mm-wave and THz [9]. For intratrain link, there are some recent papers but below 6 GHz [10, 11].

The structure of the paper is the following: in Section 2 we will describe the experiment setup, covering the environment details, the measurement setup, and the processing of the data; in Section 3 we will explain all the results obtained from the measurements, and, finally, in Section 4 a conclusion and some discussion are provided.

2. Experimental Setup

2.1. Environment. The environment for the measurement campaign is the train interior of a metro train. It is depicted in Figures 1 and 2. This vehicle under test is a Madrid Metro train of the s3000 series. It has the capacity to carry 442 persons in the four-car consist, which amounts to 132 persons on each car.

The maximum dimensions of the train are 2.3 × 3.6 × 59.7 meters, but the interior of the train has a maximum section of 2.2 m × 2.2 m. As usual in this type of trains, there are many handholds, seats, and other furniture. The seats are resin-coated reinforced with glass fiber and both the handholds and the roof are made of stainless steel covered with a 500 micrometers thick yellow painting. The floor is made of stratified rubber, the windows are made of laminated glass and the doors are of aluminum and glass like the windows' one. This layout and materials are very common in modern subway trains, with very small differences between them.

2.2. Measurement Setup. The measurements were carried out using an Agilent 8722ES Vector Network Analyzer (VNA). The approach for this VNA-based measurement is the usual one: connecting the transmitter to port 1 and the receiver to port 2, measure the s21 parameter, which is a good approximation for the channel transfer function $H(f)$ [12]. The connection of both antennas to the VNA ports was done using phase stable RTK040 wires. The length of this wire was 18 m and we used 2.4 mm connectors.

All the measurements but one were carried out using horn antennas (see Figure 3), model 22240 by FLANN, which is an antenna designed to be used in the 26.5–40 GHz, which is the band where our experiment was focused on. The gain of this antenna is 20 dB, and the variations of this parameter are bounded to 2 dB in the band of interest, which gives us a great stability. In the last measurement an omnidirectional antenna (Vivaldi, see Figure 3) was used in the receiver as a replacement of the horn antennas mentioned before.

The measured positions for the receiver (the transmitter was fixed) are depicted in Figure 2. We measured at five different transmitter-receiver distances $d = \{2, 4, 6, 9.5, 17\}$ m, moving only the receiver (in the last one the receiver is in the next train car). The height of both the transmitting and the receiving antennas was 1 m over the train floor. Both the transmitter and the receiver were placed inside the train at all time, as well as the VNA. In the measurement setup the number of dots in the 13.5 GHz wideband (26.5–40 GHz) was 1601. The processing of the data was done offline with MATLAB. As we explain in a more detailed form later in this paper, we decided to employ an automatic

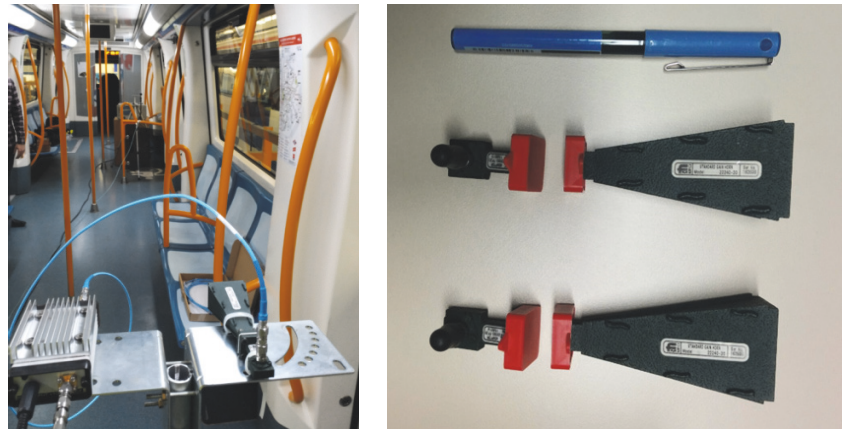

(a) (b)

Figure 3: (a) Measurement setup (from the receiver's point of view). (b) Both horn antennas are shown.

Table 1: Path loss [dB].

Distance [m]	θ					
	0°	45°	90°	135°	180°	$\overline{\text{PL}}$
2.0	29.37	61.71	63.19	60.70	57.72	54.54
4.0	36.77	61.24	61.69	60.78	62.75	56.65
6.0	40.62	60.86	61.23	62.58	62.26	57.51
9.5	45.52	53.98	65.84	64.67	65.23	59.05
17.0	54.94	54.97	66.48	66.71	66.93	62.01

clustering algorithm instead of identifying them by visual inspection.

3. Channel Model

3.1. Path-Loss. The path-loss is obtained from the measured data in the VNA. This result is the average in the entire frequency range (26.5–40 GHz) [13]. N equals 1601 which is the number of dots

$$\text{PL} = 10\log_{10}\left(\frac{1}{N}\sum_{i=1}^{N}\left|H\left(f_i\right)\right|^{-2}\right). \quad (1)$$

The obtained values are detailed in Table 1.

The path-loss increases together with the distance, both the average path-loss and the LOS ($\theta = 0^\circ$) scenario, as it was expected. Regarding the influence of the angle (θ), for $\theta = 0^\circ$ the received power is the maximum one for every measured distance, and we can see a great increase in the path-loss when we misalign the antennas $\{\theta = 45^\circ, 90^\circ, 135^\circ, 180^\circ\}$. This increase is more significant at lower distances. For example, the average path-loss increases 31.46 dB at $d = 2$ m and only 8.84 dB at $d = 17$ m. This is because at higher distances the multipath is less severe and the impact of reflections on handlers and other diffuse scatters is significantly lower (the so-called Waveguide Effect).

The variation of the path-loss for the different angles (given a fixed distance) is more or less random. However, at the highest distances $\{d = 9.5, 17$ m$\}$ the angle that experiences a lower path-loss is clearly $\theta = 45^\circ$. The reason for this is the same as before: the Waveguide Effect. To properly assess the Waveguide Effect, we have calculated the path-loss exponent (n) for 0°. The obtained value is 1.6, which is below the free-space one ($n = 2$) so, under this premises, we can conclude that we are experiencing this effect inside the train at this frequency band. The whole one-slope model is shown in

$$L_x = L_0 + 10n\log_{10}\left(\frac{d}{d_0}\right) = 29 + 16.0\log_{10}(d), \quad (2)$$

where L_x is the total losses in dB, d_0 is the reference distance, L_0 is the losses at the reference distance, n is the path-loss exponent, and d is the distance.

We also measured the path-loss at a given distance ($d = 9.5$ m) with six people moving around between the transmitter and the receiver. This impact is an average path-loss 2.28 dB higher and some fading 30 dB deep.

3.2. Ranging. If we measure the time of arrival (TOA) we can easily estimate the distance between the transmitter and the receiver

$$\tilde{d} = c \cdot \tau, \quad (3)$$

where τ is the time for the first peak in the PDP (i.e., the first path that arrives to the receiver) and c is the speed of light. In Table 2 we can see the estimated distances using this TOA-based technique to estimate the distance between transmitter and receiver. The estimation based on the LOS path is the

Table 2: Estimated distances for TOA-based method (m).

Distance [m]	θ					
	0°	45°	90°	135°	180°	
2.0	**2.11**	**2.02**	***2.51***	***2.51***	*14.09*	% error
4.0	**4.18**	*6.42*	*6.38*	*13.16*	***5.02***	<**10**%
6.0	**6.13**	***7.02***	**6.40**	***8.69***	*11.20*	***10–50***%
9.5	**9.47**	**10.00**	***10.49***	***10.91***	**9.8**	*>50*%
17.0	**16.89**	**16.89**	**17.47**		***19.24***	

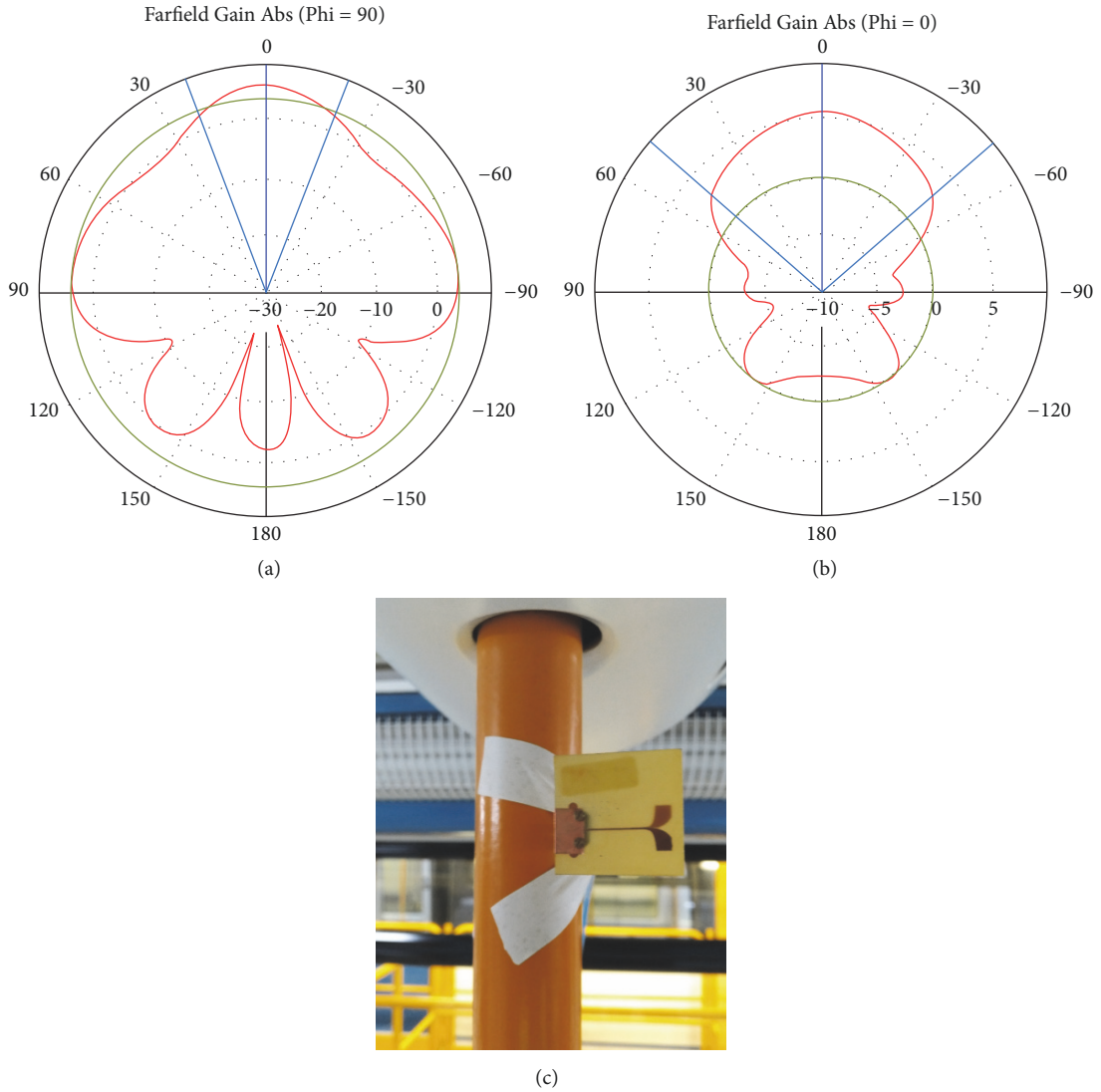

Figure 4: Radiation patterns at 25 GHz for E-plane (a) and H-plane (b) for the Vivaldi antenna. (c) The antenna is shown being installed near the top of one of the handholds of the train.

most accurate (5.56% error in the worst case and 0.35% in the best one); for $\theta = 45^\circ$ it is slightly worse and for the other angles we have large errors. This method seems to be more accurate when the distance increases (for $d = 17$ m, the error is lower than 3% for $\theta = 0^\circ$, 45°, and 90° and 13.20% for $\theta = 180^\circ$). The reason behind this good performance at higher distances is because the impact of reflections from handlers and other furniture is less significant than at lower distances.

3.3. Power-Delay-Profiles and Clustering. Regarding the Power-Delay Profiles (PDP) we have computed them for all the scenarios described in Section 2. In Figures 5–9 we can

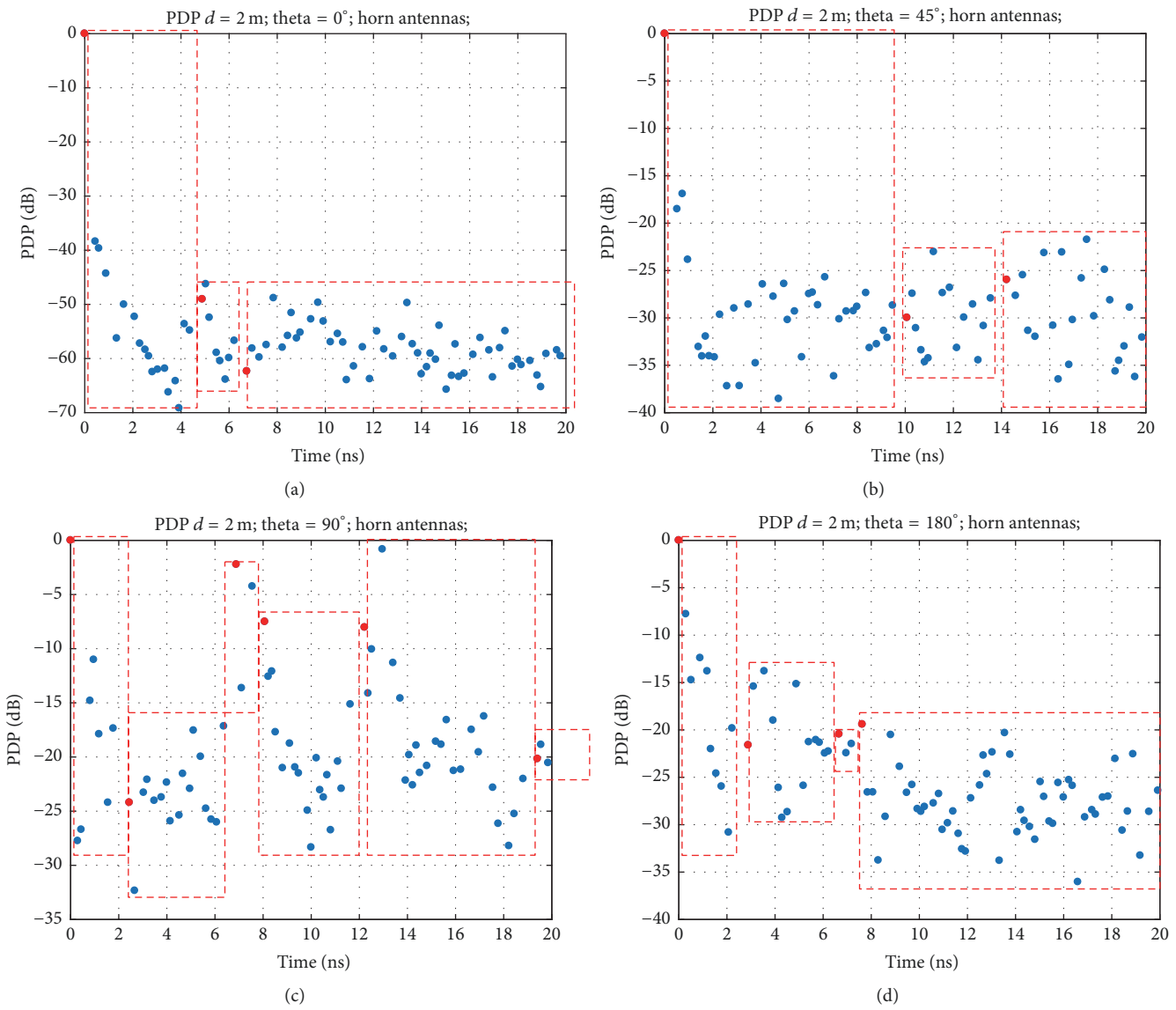

FIGURE 5: Power-Delay Profile and cluster identification for $d = 2$ m. (a) $\theta = 0^\circ$. (b) $\theta = 45^\circ$. (c) $\theta = 90^\circ$. (d) $\theta = 180^\circ$.

see the PDPs for $d = \{2, 4, 6, 9.5, 17\}$ m and an extra one for the omnidirectional antenna at a distance of $d = 4$ m.

Multipath components are clustered according to Saleh-Valenzuela [14] model and the estimation of the clusters that these multipath components form has been done using the automatic algorithm proposed in [15]. This algorithm takes into account both the amplitude and time delay to form the clusters. The usual approach to identify multipath component clusters is the visual inspection [15] but we found preferable to use an automatic algorithm. The main advantage of this algorithm is that it allows us to do a fast estimation of the clusters, and that it takes into account both time and amplitude values. Therefore, the clustering process is very dependent on the thresholds we propose (as it is acknowledged in [15]), but after some iterations, it seems to have a good performance if we look to Figures 5–11. In these figures we have highlighted in red the clusters that this algorithm has identified (dots in red are the first ray from a cluster).

For $d = 2$ m (Figure 5) we can see that the number of clusters increases with θ. For $\theta = 90^\circ$ the number of clusters increases significantly, and for $\theta = 180^\circ$ it decreases. This is an expectable result, because as we go towards a pure NLOS scenario, with many scatters between transmitter and receiver, this leads to different times of arrival (i.e., clusters).

Regarding the $d = 4$ m scenario (Figure 6) the number of clusters does not increase significantly from the previous scenario, but we have more or less the same dependence to θ. The difference between $\theta = 0^\circ$ and $\theta = 45^\circ$ is small if we visually inspect both PDPs, but for $\theta = 180^\circ$ we have more clusters in the receiver. In our opinion, this is attributable to the layout of the train that makes this PDP possible for this angle. If we employ an omnidirectional antenna in the receiver (Figure 11) we can see that we are able to see a significantly

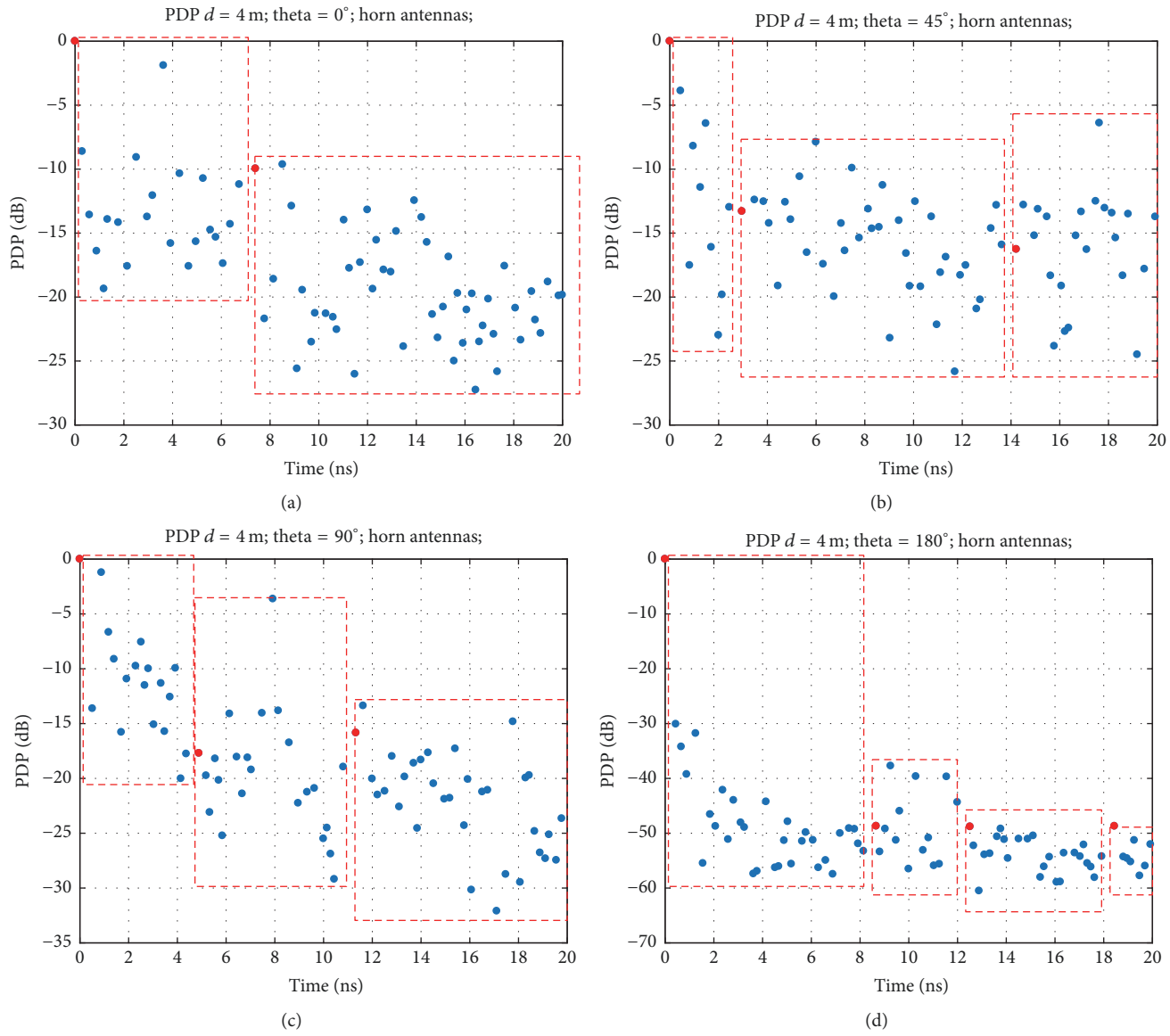

FIGURE 6: Power-Delay Profile and cluster identification for $d = 4$ m. (a) $\theta = 0^\circ$. (b) $\theta = 45^\circ$. (c) $\theta = 90^\circ$. (d) $\theta = 180^\circ$. For the $\theta = 0^\circ$ setup there is almost no room for reflections to arrive to the receiver. As we increase θ, many more clusters surge.

higher number of clusters. This is an expected result because the wider radiation pattern allows more different directions of arrival to the receiver. We still have a strong first cluster, associated with the LOS direct link plus four more clusters for the reflection through the train car.

In Figure 7 we can see the PDPs for $d = 6$ m. The number of clusters remain stable and similar to $d = \{2, 4\text{ m}\}$ for $\theta = 0^\circ$. For $\theta = 45^\circ$ we see more clusters for the same reason as before: losing the LOS link leads to more reflections due to the presence of obstacles inside the train. This is coherent with the fact that for $\theta = \{90^\circ, 180^\circ\}$ the number of clusters does not increase.

For $d = 9.5$ m (Figure 8), the estimated number of clusters is stable (and lower than before) for both $\theta = \{0^\circ, 45^\circ\}$ because we are experiencing a significant Waveguide Effect and there are many rays that are suppressed. For $\theta = \{90^\circ, 180^\circ\}$ we have the same increase in the number of clusters experienced before. So the pattern does not change from the $d = 6$ m scenario. Nevertheless, for this distance we also measured the channel with people moving randomly inside the train (between transmitter and receiver). The result can be seen in Figure 10, and the number of clusters increases significantly from any other angle at the same distance. The reason is the expected one: people act as supplementary scatters, so the PDP changes (we have more clusters, obviously). This result is very important because intratrain-based applications will work on trains with people onboard.

Finally, for $d = 17$ m (Figure 9), if we inspect visually the PDPs for the four angles considered, we can see that it does not change significantly, but the algorithm estimates 2, 6, 3, and 4, clusters for $\theta = \{0^\circ, 45^\circ, 90^\circ, 180^\circ\}$. This is perhaps the most debatable outcome of the algorithm. In this

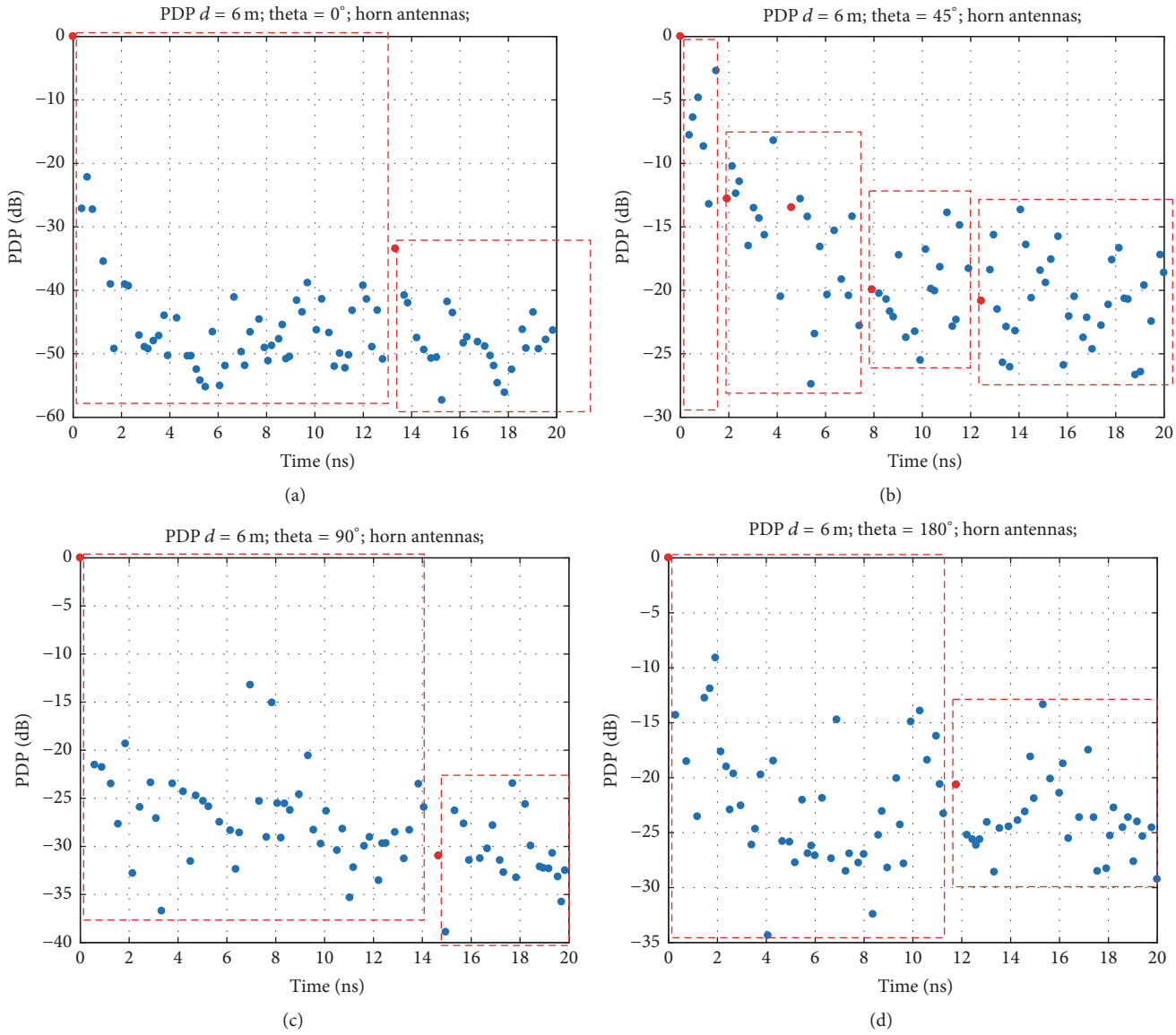

FIGURE 7: Power-Delay Profile and cluster identification for $d = 6$ m. (a) $\theta = 0^{\circ}$. (b) $\theta = 45^{\circ}$. (c) $\theta = 90^{\circ}$. (d) $\theta = 180^{\circ}$. At this distance, the clustering algorithm behaves in a very similar manner as for $d = 2$ m, but for $\theta = \{90^{\circ}, 180^{\circ}\}$ there are fewer clusters than in $d = 2$ m.

case, the distance is significantly higher than in the other scenarios, where the Waveguide Effect is dominant and the PDP is smoother (which means fewer clusters). It is also the scenario where we have less differences between angles (together with $d = 2$ m, where there were almost no scatters between transmitter and receiver). An expected result is that, at a distance like this, the power is mostly concentrated on the first cluster of rays that arrives to the receiver (this is easy to see in the $\theta = 0^{\circ}$, obviously). This is another consequence of the "Waveguide Effect."

3.4. Saleh-Valenzuela Parameters. The classical Saleh-Valenzuela (SV) model is intended for indoor scenarios and we have chosen it for its statistical nature and simplicity: it describes the channel with only four parameters (λ, Λ, γ, and Γ). Λ is the cluster arrival rate, which is assumed to follow a Poisson distribution [14], the same distribution as the ray arrival rate "λ"; "γ" is the exponential decay within a cluster; and "Γ" is the exponential decay for the whole PDP. In Table 3 we have included our estimation of these four SV parameters for all the scenarios that we have measured.

If we look at the average SV parameters in the column on the right of Table 3, we can see that we have a "slow" decay. This is because the distance between the objects that reflect the signal is very low, and all of them are very similar (metallic surfaces). That is for the "overall decay" (parameter Γ). If we look inside the clusters, we can see that they decay rapidly (parameter γ), which means a higher attenuation (due to the high frequencies) and very few reflections (apart from the first one). Anyway, this is coherent because the clustering algorithm that we chose is adequate, because the calculation of SV model parameters is very dependent on the clustering algorithm.

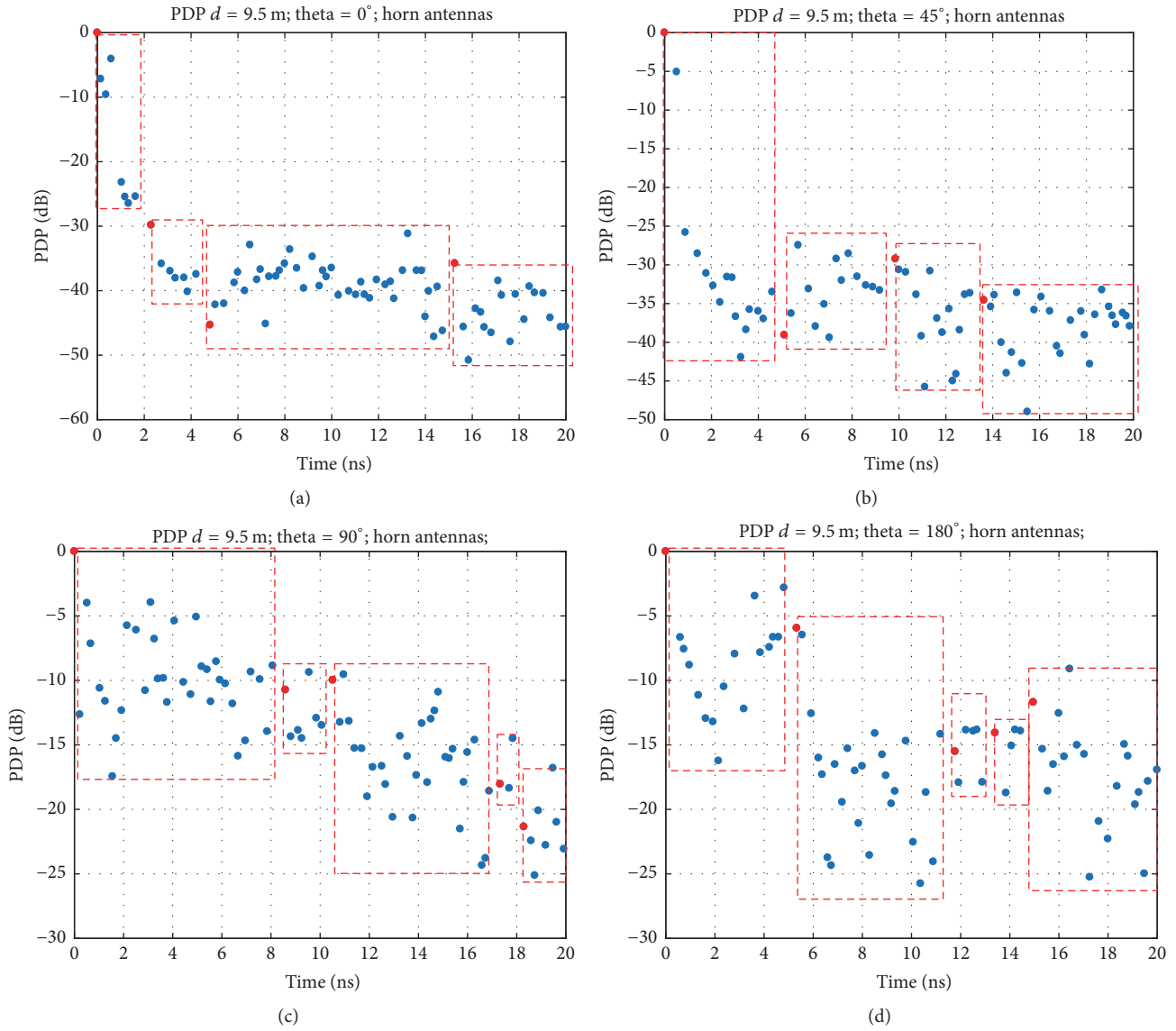

FIGURE 8: Power-Delay Profile and cluster identification for $d = 9.5$ m. (a) $\theta = 0°$. (b) $\theta = 45°$. (c) $\theta = 90°$. (d) $\theta = 180°$. We still have many clusters, especially in the angles different to 0°.

Explaining properly all the estimated SV parameters would take a lot of time, so here we will discuss some of the most significant parameters. First of all, it is noteworthy that λ (ray arrival rate) has small variations no matter in which scenario we are. This parameter is very dependent on the limitations of the measurement devices, so perhaps with a different device able to increase the number of resolvable rays this parameter could experience higher variations. The main difficulty to improve this is that the VNA employed is a state-of-the-art device, so it will take some time to achieve a better resolution in this parameter.

The cluster arrival rate (Λ) has a direct relation with the number of clusters and we have gone through this parameter in Section 3.3. Regarding the overall decay rate (Γ), it is generally higher than the cluster decay rate (γ), which is an expected result. Moreover, the clustering algorithm does not allow negative slopes (if it resolves a cluster with a negative slope; that cluster is joined to the next one) which increases—in general terms—the values of γ. If we look at some particular results, we can see that the Γ for the shortest distance ($d = 2$ m) and LOS scenario has the smallest value calculated. For higher distances and angles, the Γ increases, but the general trend is to decrease (but for $d = 2$ m), which is an expected result. It is hard to find a clear pattern in the angle variation, but a possible reason behind this behavior is that the first ray of the cluster is not always the one with more power [15]. This could lead to an underestimation of the Γ parameter.

We also took two more measurements: with people moving around inside the train ($d = 9.5$ m) and also using an omnidirectional antenna ($d = 4$ m). The Saleh-Valenzuela model parameters for the omnidirectional antenna are $\gamma =$

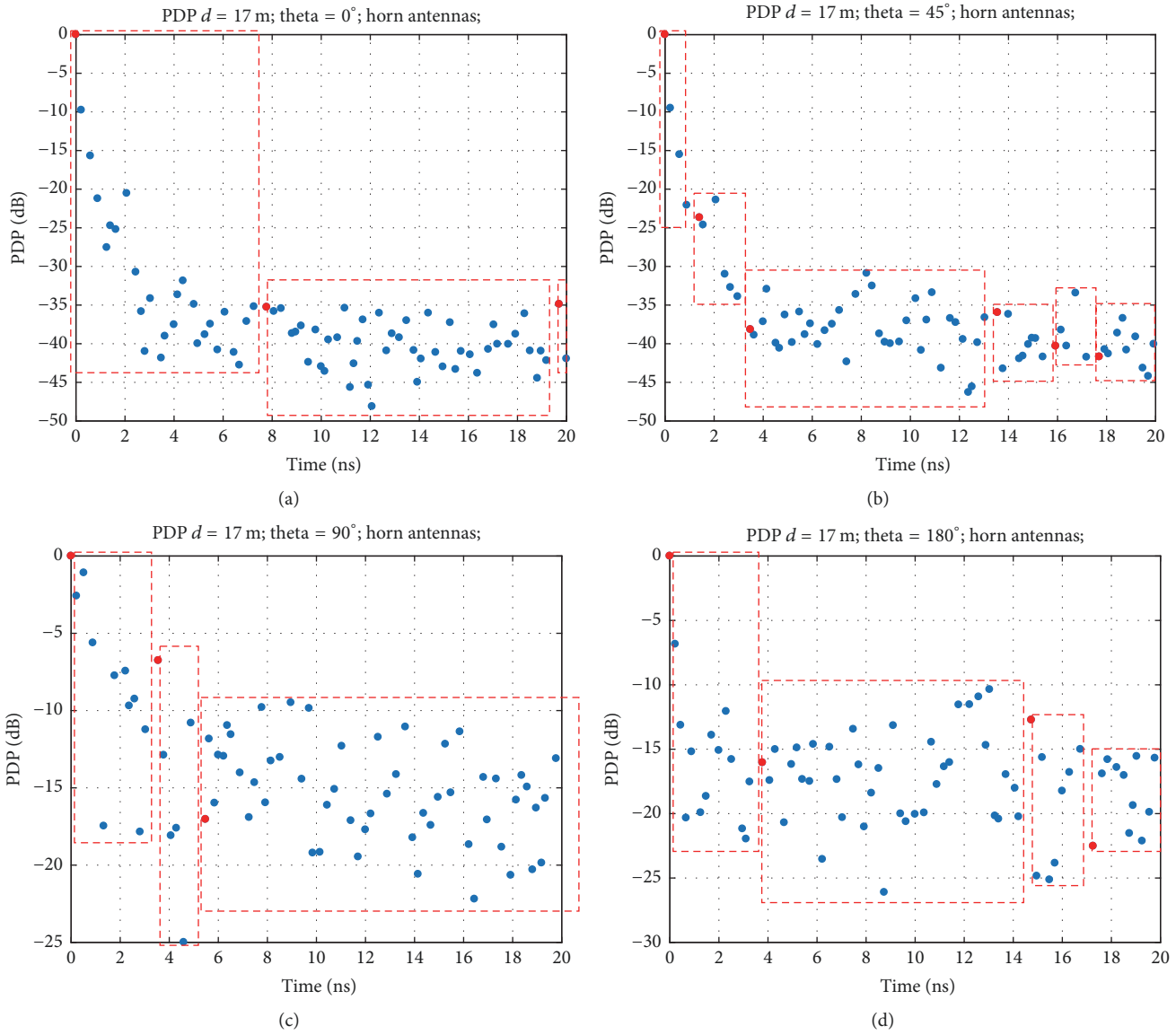

Figure 9: Power-Delay Profile and cluster identification for $d = 17$ m. (a) $\theta = 0^\circ$. (b) $\theta = 45^\circ$. (c) $\theta = 90^\circ$. (d) $\theta = 180^\circ$. The automatic algorithm identifies very few clusters for the $\theta = 0^\circ$, but many more rise if we misalign the antennas.

0.187; $\Gamma = 0.208$; $\lambda = 3.800$; $\Lambda = 0.277$. This is similar "γ" and "λ" for horn antenna in the receiver at the same distance. The apparent invariability of "λ" was discussed before and for "γ" it could be an impact of the clustering algorithm, which prevents higher variations inside a cluster, which leads to an approximately constant "γ." The number of clusters is significantly different, as the parameter "Γ" highlights, so this is coherent with the "conservative" nature (regarding "γ") of the clustering algorithm.

If we consider the difference between having people in motion between transmitter and receiver (the SV parameters are $\gamma = 0.134$; $\Gamma = 0.188$; $\lambda = 3.745$; $\Lambda = 0.277$) and not, using horn antennas and the same distance, equal to 9.5 m, we can see that we have a lower "Λ" when we have people in motion, and also a lower "Γ." It is also noteworthy that the average parameters using horn antennas (this is $\theta = \{0, 45^\circ, 90^\circ, 180^\circ\}$) are a good approximation of the scenario with an omnidirectional antenna. This is a coherent result because using an antenna like this is the same as we average the contributions from all directions. However, as we can see in Figure 4, the radiation pattern of the Vivaldi antenna is not perfectly omnidirectional, so this "averaging" process is not as precise as it could be otherwise.

4. Conclusion

The SV model can be applicable directly to an intratrain scenario, as it is an indoor scenario (the scope of the SV model). It is only necessary to estimate the parameters of the model to each environment. In particular, intratrain communications at high frequency are a high multipath environment, where SV model is intended to work.

Table 3: Saleh-Valenzuela parameters.

Distance [m]	Parameter	Angle [°]				Average
		0°	45°	90°	180°	
2.0	γ	0.058	0.172	0.264	0.124	0.155
	Γ	0.046	0.196	0.448	0.139	0.207
	λ	3.944	3.728	3.728	4.065	3.866
	Λ	0.152	0.151	0.302	0.201	0.202
4.0	γ	0.236	0.256	0.198	0.104	0.199
	Γ	0.323	0.338	0.249	0.129	0.260
	λ	3.600	3.563	3.742	3.965	3.718
	Λ	0.100	0.151	0.152	0.201	0.151
6.0	γ	0.116	0.173	0.199	0.221	0.177
	Γ	0.173	0.209	0.206	0.248	0.209
	λ	3.929	4.000	3.476	3.800	3.801
	Λ	0.101	0.250	0.101	0.100	0.138
9.5	γ	0.090	0.118	0.351	0.315	0.219
	Γ	0.136	0.140	0.395	0.429	0.275
	λ	3.700	3.576	4.115	3.650	3.760
	Λ	0.200	0.201	0.251	0.250	0.226
17.0	γ	0.145	0.117	0.200	0.187	0.162
	Γ	0.203	0.163	0.158	0.208	0.183
	λ	3.700	3.513	3.539	3.800	3.638
	Λ	0.150	0.301	0.152	0.100	0.176

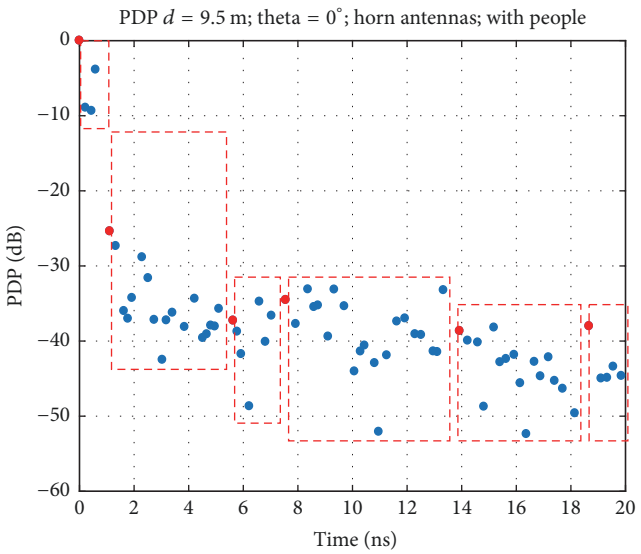

Figure 10: Power-Delay Profile for $d = 9.5$ m, $\theta = 0°$; using horn antennas and people moving around between transmitter and receiver. The effect of people increases the number of clusters and impacts the overall PDP.

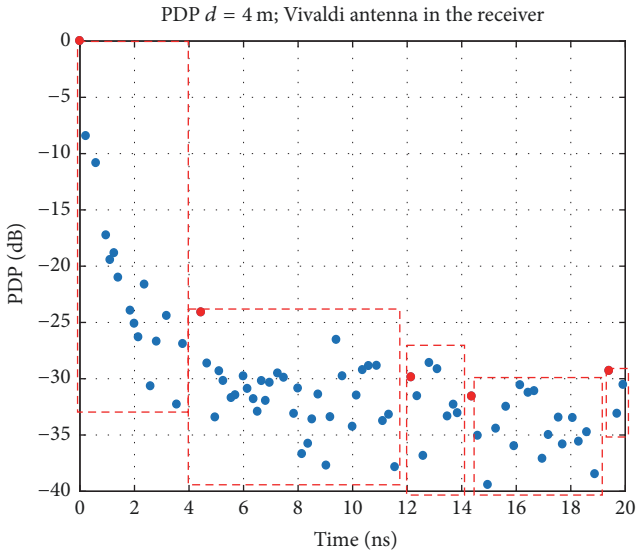

Figure 11: Power-Delay Profile for $d = 4$ m, with the Vivaldi antenna in the receiver. The automatic algorithm identifies 5 clusters.

The intratrain link is one of the most likely scenarios to require high throughputs, ultra-dense networks, and very low latencies. These three requirements are the core of 5G technologies. In this paper we have assessed this link in a region of the spectrum related to future 5G developments (26.5–40 GHz), providing estimations for the path-loss, Power-Delay Profile and Saleh-Valenzuela model parameters. We have seen the dependence of all these results on distance and angle; moreover, we have seen the impact of people moving around and also the differences coming from the radiation pattern of the receiving antenna (using an omnidirectional antenna instead of the horn antennas used in all measurements but one). The performance of the clustering

algorithm is remarkable (with some limitations, as we have discussed) and the obtained SV parameters are coherent as well.

Conflicts of Interest

The authors declare that there are no conflicts of interest regarding the publication of this paper.

Acknowledgments

Enabling 5G TEC2014-55735-C3-2-R is funded by the Spanish Ministry of Economy and Competitiveness and also is funded by the Chinese Strategic International Cooperative Project of National key R&D Plan, 2016YFE0200200.

References

[1] 5G for Europe: An Action Plan, European Commission, Brussels, 2016, https://ec.europa.eu/transparency/regdoc/rep/1/2016/EN/1-2016-588-EN-F1-1.PDF.

[2] Roll2Rail Project, http://roll2rail.eu.

[3] S.-Y. Lien, S.-L. Shieh, Y. Huang, B. Su, Y.-L. Hsu, and H.-Y. Wei, "5G New Radio: Waveform, Frame Structure, Multiple Access, and Initial Access," *IEEE Communications Magazine*, vol. 55, no. 6, pp. 64–71, 2017.

[4] G. Noh, J. Kim, H. S. Chung, B. Hui, Y. Choi, and I. Kim, "mmWave-based mobile backhaul transceiver for high speed train communication systems," in *Proceedings of the IEEE Globecom Workshops (GC Wkshps)*, pp. 1–5, Singapore, Singapore, December 2017.

[5] T. Zhou, C. Tao, S. Salous, L. Liu, and Z. Tan, "Implementation of an LTE-based channel measurement method for high-speed railway scenarios," *IEEE Transactions on Instrumentation and Measurement*, vol. 65, no. 1, pp. 25–36, 2016.

[6] J.-M. Molina-García-Pardo, M. Lienard, P. Degauque, C. García-Pardo, and L. Juan-Llácer, "MIMO Channel capacity with polarization diversity in arched tunnels," *IEEE Antennas and Wireless Propagation Letters*, vol. 8, pp. 1186–1189, 2009.

[7] S. Hairoud, P. Combeau, Y. Pousset, Y. Cocheril, and M. Berbineau, "WINNER model for subway tunnel at 5.8 GHz," in *Proceedings of the 12th International Conference on ITS Telecommunications (ITST '12)*, pp. 743–747, Taiwan, November 2012.

[8] et. Al. Ke Guan, "Broadband Channel Measurements inside Metro Station," in *Proceedings of the Progress In Electromagnetics Research Symposium Proceedings*, Guangzhou, China, 2014.

[9] K. Guan, X. Lin, D. He et al., "Scenario modules and ray-tracing simulations of millimeter wave and terahertz channels for smart rail mobility," in *Proceedings of the 11th European Conference on Antennas and Propagation (EUCAP)*, pp. 113–117, Paris, France, March 2017.

[10] I. Val, A. Arriola, P. M. Rodriguez et al., "Wireless channel measurements and modeling for TCMS communications in metro environments," in *Proceedings of the 11th European Conference on Antennas and Propagation (EUCAP '17)*, pp. 108–112, Paris, France, March 2017.

[11] A. Gonzalez-Plaza, J. Moreno, I. Val et al., "5G communications in high speed and metropolitan railways," in *Proceedings of the 11th European Conference on Antennas and Propagation (EUCAP '17)*, pp. 658–660, Paris, France, March 2017.

[12] A. Chandra, P. Kukolev, A. Prokes, T. Mikulasek, and C. F. Mecklenbrauker, "UWB measurements for spatial variability and ranging: parked car in underground garage," *IEEE Antennas and Wireless Propagation Letters*, vol. 16, pp. 1859–1862, 2017.

[13] A. Chandra, A. Prokeš, T. Mikulášek et al., "Frequency-Domain In-Vehicle UWB Channel Modeling," *IEEE Transactions on Vehicular Technology*, vol. 65, no. 6, pp. 3929–3940, 2016.

[14] A. A. Saleh and R. A. Valenzuela, "A statistical model for indoor multipath propagation," *IEEE Journal on Selected Areas in Communications*, vol. 5, no. 2, pp. 128–137, 1987.

[15] M. Corrigan, A. Walton, W. Niu, J. Li, and T. Talty, "Automatic UWB clusters identification," in *Proceedings of the IEEE Radio and Wireless Symposium (RWS '09)*, pp. 376–379, USA, January 2008.